

Simulation study of the impact of AGIPD design choices on X-ray Photon Correlation Spectroscopy utilizing the intensity autocorrelation technique

Julian Becker^{a,*}, Christian Gutt^a, Heinz Graafsma^a, on behalf of the AGIPD consortium

^a*Deutsches Elektronen-Synchrotron,
Notkestr. 85, 22607 Hamburg, Germany*

Abstract

The European XFEL, currently under construction, will produce a coherent X-ray pulse every 222 ns in pulse trains of up to 2700 pulses. In conjunction with the fast 2D area detectors currently under development, it will be possible to perform X-ray Photon Correlation Spectroscopy experiments on sub-microsecond timescales with non-ergodic systems.

A case study for the Adaptive Gain Integrating Pixel Detector (AGIPD) at the European XFEL employing the intensity autocorrelation technique was performed using the detector simulation tool HORUS. The study compares the AGIPD (pixel size of $(200\text{ }\mu\text{m})^2$) to a possible apertured version of the detector and to a hypothetical system with $(100\text{ }\mu\text{m})^2$ pixel size and investigates the influence of intensity fluctuations and incoherent noise on the quality of the acquired data.

Key words: AGIPD, simulation, XFEL, X-ray Photon Correlation Spectroscopy, aperturing, intensity fluctuations

1. Introduction

The European X-Ray Free Electron Laser (XFEL) [1] will provide ultra short, highly coherent X-ray pulses which will revolutionize scientific experiments in a variety of disciplines spanning physics, chemistry, materials science and biology. The European XFEL will provide pulse trains of up to 2700 pulses every 222 ns (600 μs in total) followed by an idle time of 99.4 ms, resulting in a supercycle of 10 Hz and 27000 pulses per second.

One of the differences to other free electron laser sources is the fast pulse repetition frequency of 4.5 MHz. Dedicated fast 2d detectors are being developed, one of which is the Adaptive Gain Integrating Pixel Detector (AGIPD) [2, 3, 4]. The development is carried out in a collaboration between DESY, the University of Hamburg, the University of Bonn (all Germany) and the Paul Scherrer Institute (PSI) in Switzerland.

The technique of X-ray Photon Correlation Spectroscopy (XPCS) provides an experimental method to probe dynamic properties of condensed matter [5] on nanometer length-scales. In XPCS experiments samples are illuminated by coherent X-ray light which results in a grainy diffraction pattern (speckle pattern). As such a speckle pattern is reflecting the exact spatial arrangement of all the particles in the beam any associated dynamics results in a fluctuation of the speckle pattern. The basic quantity determined in XPCS experiments is the intensity autocorrelation function of the speckles which measures tiny density fluctuations in the sample as a function of time and scattering vector Q . The high pulse repetition rate of the European XFEL combined with the fast frame rate of the AGIPD, will allow investigations using the XPCS technique on the sub-microsecond timescale.

Depending on the dynamic phenomena of interest and the associated time scales different technical realizations of photon correlation spectroscopy exist. For the very fast time scales in the regime of 10^{-12} to

*Corresponding author

Email addresses: Julian.Becker@desy.de (Julian Becker)

Preprint submitted to Journal of Instrumentation

July 27, 2022

10⁻⁹ seconds the split and delay technique can be applied. To study effects on the time scale of 10⁻⁶ to 10⁰ seconds, which are relevant in soft matter or biological systems, sequential XPCS is performed [6].

Photon correlation experiments are limited by their signal to noise ratio (S/N or SNR) [7]. An important aspect of the SNR in XPCS experiments is the ability of the X-ray detector to resolve the speckle pattern. It can be shown that an optimal signal to noise ratio is achieved in situations where the speckle size equals the pixel size [8]. As XPCS seeks to measure dynamic sample properties the X-ray beam needs to illuminate the same sample spot several times. This implies that sample distortions (especially sample heating) due to interactions with the illuminating beam are reduced as much as possible by using a large beam size. The speckle size is inversely proportional to the beam size and therefore speckle sizes will be small for XPCS experiments at XFEL sources. The pixel sizes of the fast 2D-detectors under development will be larger than the expected speckle sizes. The question to what extent this mismatch affects the SNR and the quality of the intensity correlation functions is investigated in this paper. We present simulations of a prototypical XPCS experiment for different detector systems in otherwise identical situations. The study is limited to small angle scattering experiments and shows the influence of the detector system on the SNR which is commonly neglected.

Furthermore, a method of reducing the effective pixel size by aperturing the sensitive area of each pixel is investigated in this study. Aperturing pixels produces a detector consisting of smaller pixels, which are isolated and separated from each other. Compared to adjacent small pixels this eliminates charge sharing and allows to sample a larger area with the same number of pixels. On the other hand the fraction of sensitive area over total area is greatly reduced.

This study is the first investigating the performance of the AGIPD and the influence of certain design choices on the data quality of the experiment. A system level simulation study using an XPCS case for the DSSC¹ project can be found in literature [9].

2. Simulation of a prototypical XPCS experiment at the European XFEL

All simulations have been performed within the IDL framework² using version 7.1. The simulations consist of three independent stages treating the real space system, the diffraction image generation and the detector response simulation. The stages are explained in detail below. The simulations are followed by a data evaluation step, which is explained in section 3.

2.1. Real space system

The simulated diffraction patterns were based on the evolution of a real space system. For ease of simulation the simulated real space system consisted of particles hopping on a two dimensional grid. The particles did not interact with each other and could occupy the same grid position. Per simulation step (Δt) each particle could move by ± 1 grid position with a probability of 1 % in each of the dimensions independently. Particles leaving the grid on one side were replaced by particles entering on the opposite side. In total 5000 particles were simulated on a square grid of 2000×2000 points. The initial distribution of particles was random.

2.2. Generation of diffraction images

All calculations were done image-based. Thus for each simulation step a real space image was generated. The real space image had the same size as the simulation grid and each image pixel was assigned the number of particles at the corresponding grid point.

2.2.1. Speckle size, illumination function and Fourier transform

The speckle size S is usually given by the following expression:

¹The DEPFET Sensor with Signal Compression (DSSC) project and Large Pixel Detector (LPD) project are the other two projects developing a dedicated detector for experiments at the European XFEL.

²IDL stands for Interactive Data Language and is distributed by ITT Visual Information Solutions. For more information visit <http://www.itervis.com/>

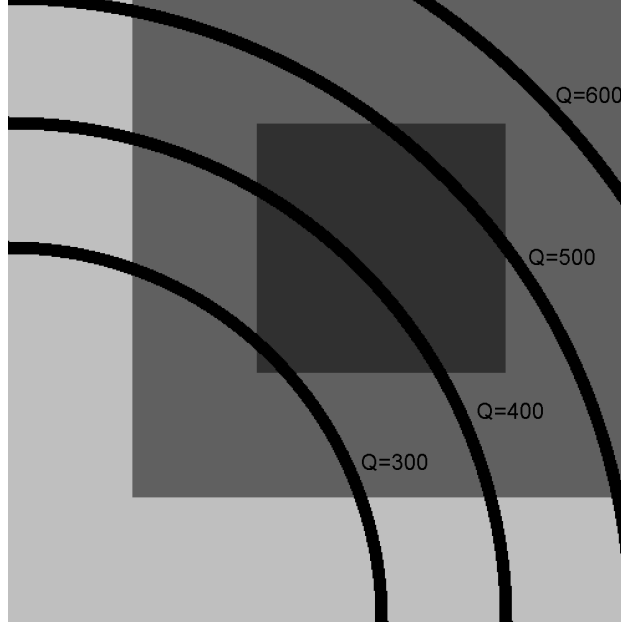


Figure 1: Regions of the diffraction pattern and their assignment in this study. Light gray: discarded pixels due to possible structure and form factors. Medium and dark gray: pixels used for all studies of $(200\text{ }\mu\text{m})^2$ detectors and small ROI investigations of $(100\text{ }\mu\text{m})^2$ detectors. Dark gray: pixels used for studies of $(100\text{ }\mu\text{m})^2$ detectors and large ROI investigations. Pixels assigned to the exemplary Q bins of 300, 400, 500 and 600 units have been marked black.

$$S \approx \frac{\lambda L}{D} \quad (1)$$

with λ being the wavelength of the illuminating light, L the sample to detector distance and D the size of the illuminating light beam. Therefore an illumination function, which corresponds to the spatial distribution of the primary beam, is needed to define the speckle size in the detector plane.

The complex wave field in the detector plane E_{diff} was defined as:

$$E_{diff} = FT \{F_{rs} * F_{ill}\} \quad (2)$$

where F_{rs} is the real space image and F_{ill} the illumination function with FT denoting the discrete Fourier transform (FFT algorithm) and $*$ indicating pixel by pixel multiplication. The illumination function was assumed to be a Gaussian function centered on the image center with a sigma corresponding to one eighth of the image size.

To remove the structural artifacts of the square image the first 200 pixels in x and y direction were discarded. The removed area is shown in light gray in Figure 1.

A Fourier transform of real values is symmetric around the Nyquist frequency, as indicated by Friedel's Law. As $E_{diff}(Q) = E_{diff}^*(-Q)$, areas symmetric to Figure 1 were removed from the complex wave field, leaving data from a region of 800×800 pixels for further processing, shown in medium and dark gray in Figure 1. The intensities from an exemplary wave field are shown in the left image of Figure 2 and exhibit no structure and form factor effects.

The upper right image of Figure 2 shows a histogram of the intensities of the complex wave field with a bin size of one hundredth of the average intensity $\langle I \rangle$. The expected negative exponential distribution [10] for fully coherent illumination is clearly reproduced and the most probable intensity value is zero. The apparent spread towards large $I / \langle I \rangle$ is due to the finite number of image pixels.

The lower right image of Figure 2 shows the average normalized spatial autocorrelation function ACF of the intensities along the x direction averaged over the y direction defined by:

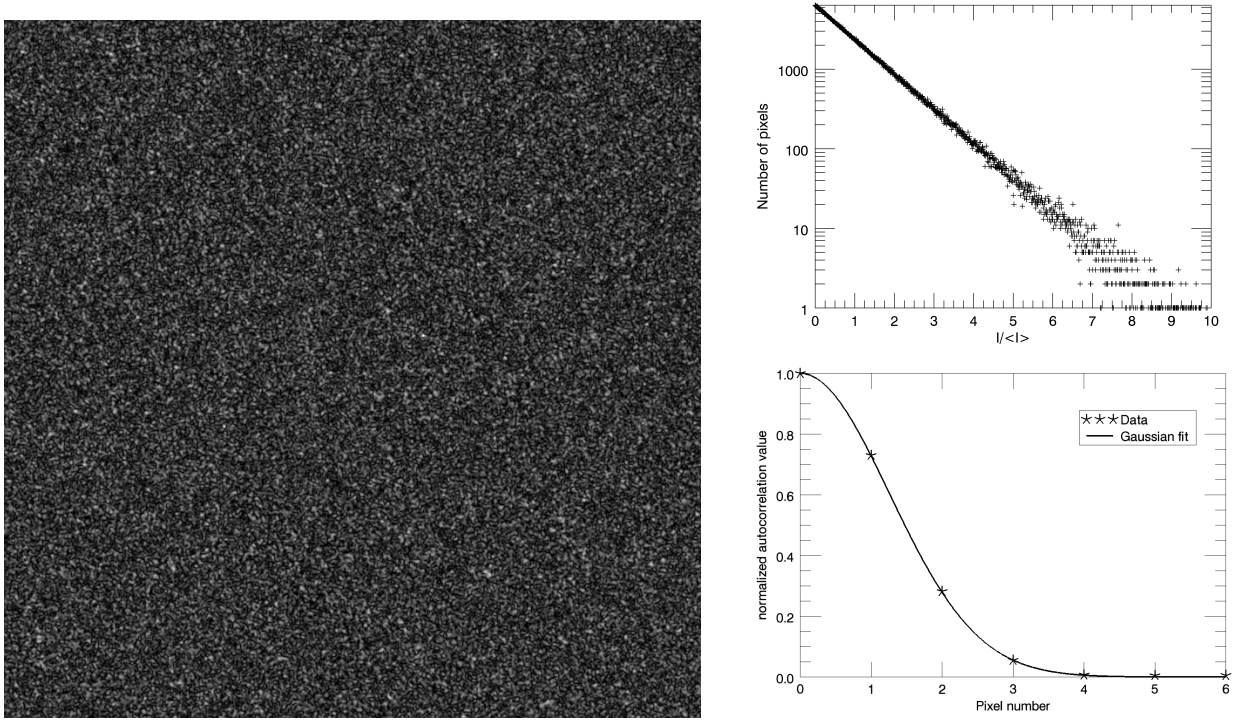


Figure 2: The left image shows the intensity distribution of one exemplary Fourier transform. No structure and form factor can be observed. The upper right image shows the histogram of the intensity distribution, binned with a bin size of $0.01 < I >$. The lower right image shows the autocorrelation function along the x axis averaged over the y axis, thus revealing the average speckle shape. The speckle shape is excellently matched by a Gaussian fit with a sigma of 1.25 pixels.

$$ACF(\Delta R) = \frac{1}{N_y} \sum_{l=0}^{N_y-1} \frac{\sum_{k=0}^{N_x-\Delta R-1} (I_{k,l} - \langle I \rangle_l)(I_{k+\Delta R,l} - \langle I \rangle_l)}{\sum_{k=0}^{N_x-1} (I_{k,l} - \langle I \rangle_l)^2} \quad (3)$$

where ΔR is the inter pixel distance, N_x and N_y are the number of pixels along the corresponding direction, $I_{k,l}$ the intensity in the indicated pixel and $\langle I \rangle_l$ the average intensity in the corresponding line.

By calculating the average normalized spatial autocorrelation function the speckle shape and size was determined independently from the knowledge of the illumination function. The speckle shape corresponds excellently to the Gaussian fit with a sigma of 1.25 pixels³. Exchanging x and y direction in the evaluation yielded identical results, indicating symmetric speckles.

Speckle positions can be misaligned with the detector pixel grid. In order to simulate this, 2 by 2 pixels of the Fourier transform were assigned to each $(100 \mu\text{m})^2$ pixel area. Correspondingly $(200 \mu\text{m})^2$ area were assigned 4 by 4 pixels of the complex wave field. The sub-pixel position information gained by this procedure was used in the detector simulation step.

2.2.2. Intensity normalization and fluctuation, image quantization and incoherent noise

The diffraction pattern impinging on the detector consists of discrete photons. This discrete photon distribution F_γ was generated in the following way:

$$F_\gamma = S \left\{ \langle I \rangle_d R_{fluct} \frac{I(E_{diff})}{\langle I(E_{diff}) \rangle} \right\} + F_{noise} \quad (4)$$

³As the Fourier transform is oversampled and one pixel length corresponds to $50 \mu\text{m}$, this results in a sigma of $62.5 \mu\text{m}$ and a full width at half maximum of $147.2 \mu\text{m}$ for the speckles in this simulation study.

where $S(X)$ is the image quantization procedure explained below, $\langle I \rangle_d$ the desired average intensity, R_{fluct} the intensity fluctuation factor explained below, $I(E_{diff}) = |E_{diff}|^2$ the intensity distribution in the detector plane, $\langle I(E_{diff}) \rangle$ the average intensity in the detector plane and F_{noise} the additional incoherent noise explained below.

The fully coherent wave field is ergodic⁴. In order to quantize the photon field (denoted by $S(X)$), the photons were sampled according to the negative binomial distribution expected for its spatial distribution [10], using the floating point pixel intensity as the expected value $\langle I \rangle$:

$$P(I) = \frac{\Gamma(I+M)}{\Gamma(M)\Gamma(I+1)} \left(1 + \frac{M}{\langle I \rangle}\right)^{-I} \left(1 + \frac{\langle I \rangle}{M}\right)^{-M} \quad (5)$$

where I is a discrete number of photons, $P(I)$ the probability of realizing I photons and M the number of modes in the image. $\Gamma(x) = (x-1)!$ denotes the gamma function. Thus, for the fully coherent case ($M = 1$) investigated in this study, equation 5 simplifies to:

$$P(I) = \frac{1}{1 + \langle I \rangle} \left(\frac{\langle I \rangle}{1 + \langle I \rangle}\right)^I \quad (6)$$

The intensity fluctuation factor R_{fluct} was either set to unity (no fluctuations) or sampled randomly from a Gaussian distribution with a mean of 1 and an rms of 0.1. The factor does not simulate intensity fluctuations directly, but rather remaining uncertainties after accounting for intensity fluctuations. Intensity fluctuations can be accounted for in the determination of the autocorrelation function by weighting images, however the most probable value of zero photons cannot be scaled, hence creating uncertainties.

The incoherent noise F_{noise} added after the quantization process was either zero or considered Poissonian with a probability of 1/400 per pixel of the Fourier transform. This translates to a noise photon probability of 1/100 per $(100 \mu\text{m})^2$ detector area. Thus for an average intensity of 0.01 the S/N from the experiment itself is 1. As the noise of the detection process was simulated separately (see below) this completely random noise can be considered a high estimate of fluctuations of an otherwise constant background distribution.

2.3. Detector response

In order to evaluate the effects of the investigated detector systems (detailed below), the same photon distributions F_γ were taken as input for the different detector systems.

2.3.1. Simulated detector systems

To evaluate the influence of different detector choices the following detector systems were simulated:

- Ideal detector systems with $(100 \mu\text{m})^2$ and $(200 \mu\text{m})^2$ pixel size.
- The Adaptive Gain Integrating Pixel Detector (AGIPD) featuring $(200 \mu\text{m})^2$ pixel size.
- A Modified AGIPD using Aperturing Techniques (MAAT), which was identical to the AGIPD, but completely insensitive to photons which are closer than $50 \mu\text{m}$ to a pixel boundary⁵, which resulted in an effective pixel size of $(100 \mu\text{m})^2$.
- A Reduced Amplitude SEnsing System (RAMSES), which was a hypothetical detector which sacrificed most of the AGIPD functionality (e.g. the gain switching) but featured $(100 \mu\text{m})^2$ pixel size.

⁴In very simplified terms: An ergodic system shows the same average behavior when probed an infinite number of times sequentially as an infinite number of identical systems would show when probed once.

⁵For real applications this could e.g. be realized by post-processing a tungsten grid of $10 \mu\text{m}$ thickness on the entry window of the detector.

2.3.2. The Adaptive Gain Integrating Pixel Detector (AGIPD)

AGIPD is based on the hybrid pixel technology. A newly developed Application Specific Integrated Circuit (ASIC) will feature in each pixel a dynamic gain switching amplifier (to cope with the high dynamic range) and an analogue memory capable of storing approximately 300 images at the desired 4.5 MHz speed.

The AGIPD will feature a pixel size of $(200\text{ }\mu\text{m})^2$ and a silicon sensor with a thickness of $500\text{ }\mu\text{m}$. The area of $(200\text{ }\mu\text{m})^2$ is needed to realize in-pixel electronics which fulfill the requirements for detectors at the European XFEL [2, 3]. The image data is read out and digitized in the gap between two pulse trains.

2.3.3. Physical constraints precluding the realization of an ideal detector

Due to the special pulse structure of the European XFEL it is necessary to store the acquired images inside the pixel logic during the pulse train. A compromise has to be found between a large pixel area, so many images can be stored, and small pixel area, i.e. high spatial resolution.

Additionally effects of the limited stopping power of silicon and the charge transport in the sensitive volume come into play. The chosen sensor thickness of $500\text{ }\mu\text{m}$ provides a quantum efficiency exceeding 85% for 12 keV photons. After a photon is absorbed, a cloud of charge carriers is created, which expands before reaching the readout electrode and may cause charge sharing between pixels.

The actual shape and size of this cloud is influenced by many parameters⁶. In this study the collected charge is approximated as following a Gaussian distribution with a width depending of the square root of the distance to the electrode [11]. To minimize charge sharing between the pixels, the charge cloud size should be small compared to the pixel size⁷. Given the material properties of a typical silicon detector of $500\text{ }\mu\text{m}$ thickness and using recent determinations of the charge carrier mobilities [13], typical cloud sizes (full width at half maximum) are in the range of $20\text{ }\mu\text{m}$. Thus reducing the pixel size from the current value of $(200\text{ }\mu\text{m})^2$ will result in less benefit than expected from geometric considerations.

2.3.4. HORUS

The detector response was calculated using the HORUS software described in [14]. The entry window of the sensor was included as $3\text{ }\mu\text{m}$ of dead, silicon equivalent, material for all systems, which is about twice of the value foreseen for AGIPD at the moment. The total noise was assumed to have an equivalent noise charge of approximately 300 electrons, which is about double the value determined from ASIC simulations [3] and roughly the value measured on a test assembly using a microstrip sensor.

To increase the simulation speed several approximations were used:

- Any parallax effects were ignored. This is a reasonable approximation, as the sample to detector distance for XPCS experiments at the European XFEL will probably be 10 m and more.
- Any effects originating from sensor edges and module gaps were ignored. Although in the final detector system these effects cannot be avoided, for XPCS data evaluation it is possible to mask areas exhibiting these effects and exclude them from the data analysis.
- Effects produced by high instantaneous charge densities (so called plasma effects) are not simulated by HORUS, and thus were not included in this study. Neglecting these effects is a reasonable approximation, as the intensities in XPCS experiments are usually low and plasma effects are expected to show only for intensities larger than 250 photons per pulse per $(100\text{ }\mu\text{m})^2$ area [15, 16].

For simulation purposes the ideal detectors were realized by rebinning the oversampled photon field to the corresponding pixel size, as an ideal detector will detect all the photons on the detector area without any distortions.

⁶A non-exhaustive list includes: bias voltage, sensor doping, number of charge carriers, electrode geometry and exact initial position.

⁷For XPCS applications charge sharing should be avoided if possible, as the signal of adjacent pixels would be correlated, increasing the effective pixel size. It should be noted that for very low intensities (low pixel occupancies) charge sharing is beneficial, as event-by-event correlations can be performed [12].

The response of the MAAT was calculated in an identical way as for the AGIPD, but photons hitting the insensitive regions are discarded in F_γ .

The RAMSES was modeled using the AGIPD parameters, except that the pixel size in the simulations was $(100 \text{ } \mu\text{m})^2$, effectively quadrupling the number of pixels in the simulation (as the same Q space is covered).

2.3.5. Region of interest

There will be experimental cases, where the entire region of interest can be sampled with the detector area. For these cases the detector performance is limited by the pixel density and similar total areas covered by $(100 \text{ } \mu\text{m})^2$ and $(200 \text{ } \mu\text{m})^2$ pixels had to be compared. These cases are labeled as cases with small Region Of Interest (sROI) in the rest of this study.

For cases where the potential region of interest exceeds the detector area $(100 \text{ } \mu\text{m})^2$ and $(200 \text{ } \mu\text{m})^2$ systems with an identical number of pixels had to be compared. The Q region for the simulated small pixel detectors was limited to the same number of pixels that was used for the large pixel detectors, shown as the dark gray area in Figure 1. These cases are labeled as cases with large Region Of Interest (lROI).

It should be noted that, translated to real physical systems, the Q vector units in the small and large ROI cases would therefore have different meanings.

3. Data evaluation

The simulation was performed multiple times for each intensity, simulating the data acquisition of five independent⁸ pulse trains ($N_{tr} = 5$), thus the overall data set consisted of 5×300 frames ($N_f = 300$) per detector type per intensity point.

3.1. The intensity autocorrelation function

The intensity autocorrelation function (g_2 function) is both a measure of the correlation time and the contrast. For ideal circumstances, which are not realized here, the g_2 function would be a function monotonically decreasing from a value of 2 for $k\Delta t \rightarrow 0$ to a value of 1 for $k\Delta t \rightarrow \infty$. The functional form is determined by the sample dynamics and the correlation time constant can be extracted, the scaling is a measure of the optical contrast.

For the data evaluation the g_2 function was calculated individually for each pixel p according to the following formula⁹:

$$g_2(p, k\Delta t) = \frac{1}{N_{tr}} \sum_{tr=0}^{N_{tr}-1} \frac{1}{N_f - k} \sum_{i=0}^{N_f-k-1} \frac{I_{p,tr}(i\Delta t) I_{p,tr}((i+k)\Delta t)}{\langle I_p \rangle^2} \quad (7)$$

where the average intensity of pixel p ($\langle I_p \rangle$) is calculated as:

$$\langle I_p \rangle = \frac{1}{N_{tr}} \sum_{tr=0}^{N_{tr}-1} \frac{1}{N_f} \sum_{i=0}^{N_f-1} I_{p,tr}(i\Delta t) \quad (8)$$

and Δt is the time difference between frames and $I_{p,tr}(i\Delta t)$ denotes the intensity in pixel p in frame i of pulse train tr . This procedure yielded a g_2 function for each pixel of each investigated average intensity and detector type.

Especially at very low intensities there were pixels which did not detect any photon in the whole series. To avoid division by zero (as $\langle I_p \rangle = 0$) the g_2 function for these pixels was set to zero.

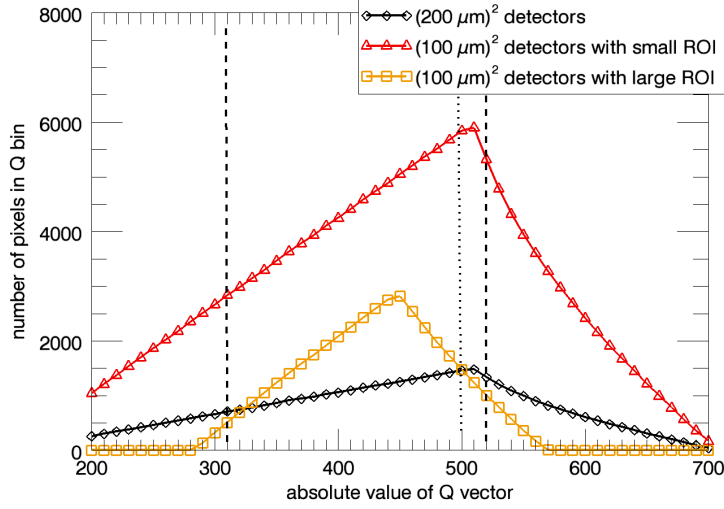


Figure 3: Number of pixels as function of Q value for the simulated detector systems. The Q range between the dashed lines has been used for Q averaging, as explained in the text. The dotted line is the Q vector shown in Figures 4, 5, 10 and 11.

3.2. Q space binning and azimuthal average

Azimuthal averages (ensemble averages) were calculated by binning pixels that fulfilled the condition $Q - \Delta Q \leq Q(p) < Q + \Delta Q$, where $Q(p)$ was the absolute value of the Q vector for pixel p and $2\Delta Q = 10$ was the bin size. Exemplary Q space bins are shown in Figure 1, the number of binned pixels as function of Q value is shown in Figure 3. The ensemble averaged $g_2(Q, k\Delta t)$ function is the average of all $g_2(p, k\Delta t)$ functions in the corresponding Q space bin.

As an example the resulting $g_2(Q, k\Delta t)$ functions at a fixed Q value of 500 units as a function of average intensity are shown for the ideal $(100 \mu\text{m})^2$ detector in Figure 4 and for AGIPD and MAAT in Figure 5.

Figure 4 shows the expected exponential decay of the autocorrelation function with increasing lag time. The maximum value for low lag times is approximately 1.7, thus below the theoretical maximum value of 2, as the experimental contrast is smaller than one. For lag times beyond 100 the function falls below 1.0 and increases again towards larger lag times. This behavior is commonly observed when evaluating the intensity autocorrelation function on a limited set of frames and would disappear if more frames were imaged in sequence. The apparent contrast decreases as the intensity decreases. At the lowest intensities the images become uncorrelated as they are dominated by noise, correspondingly the g_2 function appears flat.

Figure 5 shows the exponential decay of the autocorrelation function for the AGIPD and MAAT. The features seen for the ideal system are observed here as well. The maximum value for AGIPD and MAAT at low lag times is approximately 1.3 and 1.7, thus MAAT produces a similar contrast to the ideal $(100 \mu\text{m})^2$ detector. When compared to the g_2 functions shown in Figure 4, the AGIPD curves appear smoother, as the larger pixel size averages over a larger area, while the MAAT curves appear less smooth, as the g_2 function is calculated from less detected photons. This is especially prominent at the lowest intensities.

3.3. Fit to the g_2 function

Each ensemble averaged $g_2(Q, k\Delta t)$ function was fitted with the following function to evaluate the performance of the different detector systems:

⁸In the simulations each train used a new random number sequence.

⁹The shown equations use the commonly employed normalization scheme. The data was also analyzed using the symmetric normalization scheme discussed in [17], however the results were worse then for the commonly employed normalization scheme and are therefore not shown here.

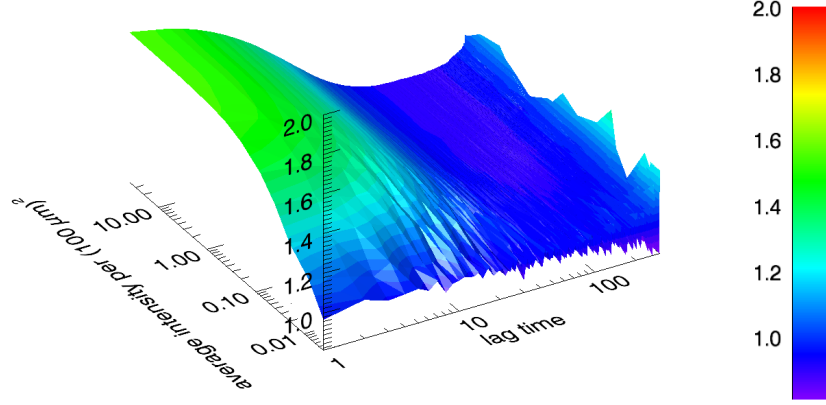


Figure 4: Resulting g_2 functions at a fixed Q of 500 units as function of average intensity. Results were obtained for the ideal $(100 \mu\text{m})^2$ detector for small ROIs, the results include all noise sources mentioned in the text. The apparent increase of the g_2 at very large lag times is an artifact induced by the finite number of images.

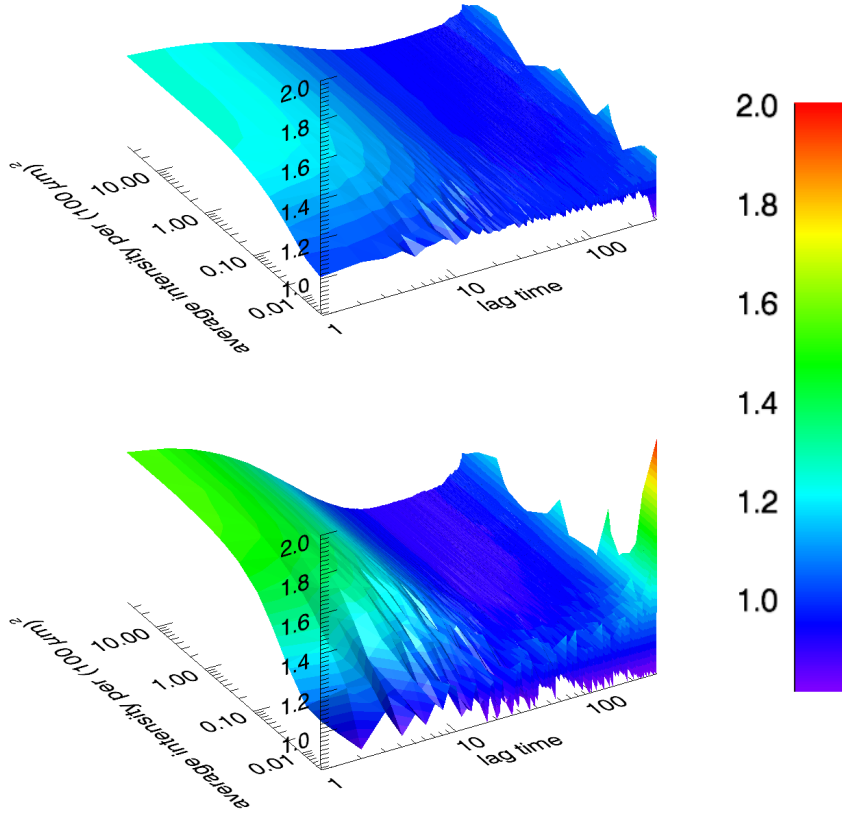


Figure 5: Resulting g_2 functions at a fixed Q of 500 units as function of average intensity. The upper image shows the results for the AGIPD, the lower image shows the results for the MAAT. The results include all noise sources mentioned in the text. The apparent increase of the g_2 at very large lag times is an artifact induced by the finite number of images.

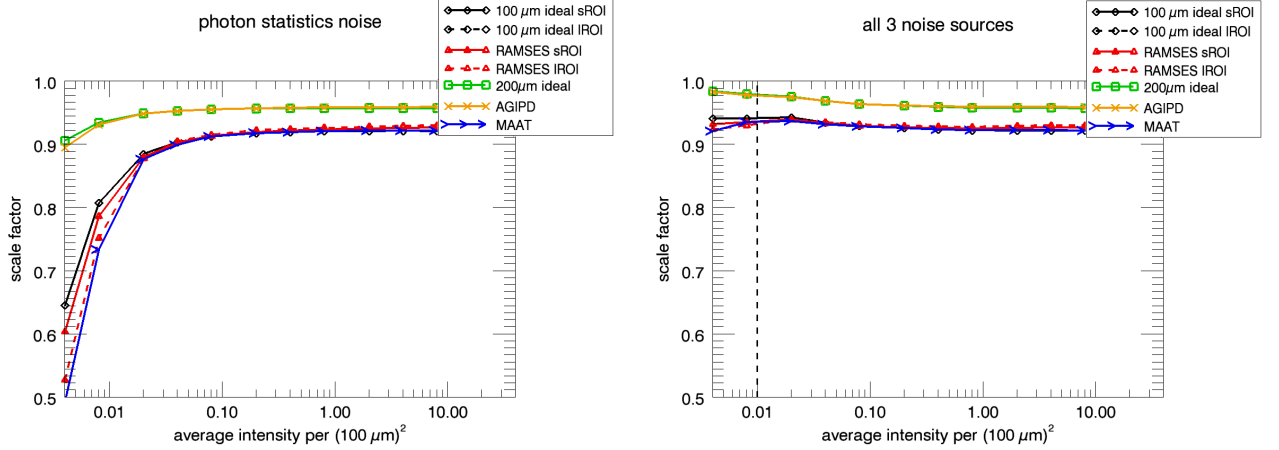


Figure 6: Average scaling parameter for all systems. The left shows the results for photon statistics noise only, the right image shows the results including all mentioned noise contributions. The dashed vertical line indicates the average intensity of F_{noise} .

$$g_2(Q, k\Delta t) = S(Q) \{C(Q) \exp(-2\Gamma(Q)\tau) + 1\} \quad (9)$$

where $\tau = k\Delta t$ is the lag time, $S(Q)$ a scaling parameter, $C(Q)$ the optical contrast and $\Gamma(Q)$ the inverse of the correlation time τ_c .

For the dispersion relation $\Gamma(Q)$ it was assumed that $\Gamma(Q) = C_{disp}Q$, and likewise $\tau_c = (C_{disp}Q)^{-1}$.

The scaling parameter $S(Q)$ was necessary to compensate for g_2 functions with a vanishing value, especially at low intensities. It can be calculated analytically as $1 - (N_{<I_p>=0}/N_Q)$, where $N_{<I_p>=0}/N_Q$ is the fraction of pixels in a given Q bin which have zero intensity in all frames of a given pulse train.

4. Results

The influence of the intensity fluctuation factor R_{fluct} in Equation 4 on the results was found to be negligible. Thus only photon statistics noise ($R_{fluct} = 1.0$ and $F_{noise} = 0$) results will be compared to results including all noise sources.

Using the Fourier transform to generate diffraction patterns implies an infinite coherence length, both longitudinal and transverse, thus the commonly observed drop in contrast at high Q values is neglected. As a consequence there is little change in contrast and scaling factor as function of Q value. Thus the fit results were averaged for Q values between 310 and 520 units.

The Q range between 310 and 520 units has been chosen as it excludes Q vectors with low statistics towards the edge of the sensitive area for large regions of interest. The $(200 \mu\text{m})^2$ detectors and small ROI cases have been restricted to the same Q range to have a comparable data set, although the errors for these systems could have been reduced using the additional information available at other Q values.

4.1. Scaling parameter

Generally the scaling parameter shown in Figure 6 behaves as expected and explained in section 3.3. The average scaling parameter for the $(200 \mu\text{m})^2$ systems is always larger than for the $(100 \mu\text{m})^2$ system as the speckle size stays constant.

The scaling factor can be interpreted as the fraction of non-zero pixels when summing together all images. Which can be clearly observed as without noise, the scaling factor is decreasing at low intensities.

When summing together all images the expected value for noise photons is $\lambda = N_F/P_{noise} = 3$ photons per $(100 \mu\text{m})^2$, so an average scaling factor of $1 - P_\lambda(0) \approx 0.95$ is expected when noise is present and also observed for low intensities.

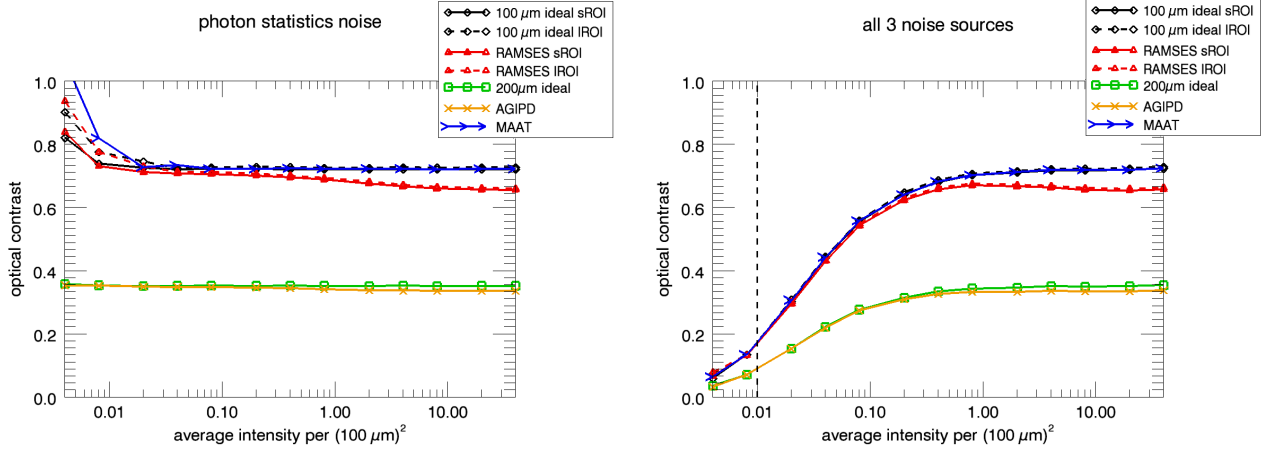


Figure 7: Average optical contrast for all detector systems as function of intensity. The left image shows the results for photon statistics noise only, the right image shows the results including all mentioned noise contributions. The dashed vertical line indicates the average intensity of F_{noise} .

4.2. Optical contrast

Figure 7 shows the Q averaged results for the optical contrast. When F_{noise} is included in the simulations the optical contrast decreases once $\langle I \rangle / I_{noise} \lesssim 100$ ($\langle I \rangle \approx 1$), while it stays almost constant without noise. For $F_{noise} = 0$ and very low intensities the contrast apparently increases due to the biasing effect of the scaling factor. However this additional contrast did not improve the data quality, as the scaling factor decreased strongly.

Figure 7 shows that, except for MAAT, the real systems show a lower contrast than the ideal ones, independent of the noise. At low intensities the difference vanishes. This reduced contrast was caused by charge sharing events, which correlate the pixel values. Charge sharing is excluded for MAAT by its design.

The fact that the results for MAAT reproduce the results for an ideal $(100 \mu\text{m})^2$ system, indicate that the detector noise and quantum efficiency do not influence the data quality.

For the ideal systems the contrast was given by $C(\langle I \rangle) \approx C_{geom}(1 - I_{noise}/\langle I \rangle)$, where C is the determined contrast and C_{geom} the contrast expected from geometric estimations:

$$C_{geom} = \frac{1}{1 + \frac{P^2}{S^2}} \quad (10)$$

with P being the linear pixel size and S the full width at half maximum of the speckles.

The geometric estimate and the results of the ideal systems at the highest intensity are in good agreement (0.68 and 0.72 or 0.35 and 0.36 for $(100 \mu\text{m})^2$ or $(200 \mu\text{m})^2$ systems, respectively).

4.3. Correlation time

Figure 8 shows the inverse correlation time $\Gamma(Q)$ for the ideal $(100 \mu\text{m})^2$ detector and small ROIs as function of Q vector and intensity.

Overall, the correlation time was observed to be approximately inversely proportional to the Q vector ($\Gamma(Q) = C_{disp}Q$, likewise $\tau_c = (C_{disp}Q)^{-1}$). The Q averaged results for the dispersion constant C_{disp} are displayed in Figure 9 for all simulated detector systems.

For purely diffusive systems $\Gamma(Q)$ should be proportional to Q^2 , but the investigated jump diffusion system did not show such a behavior. Literature shows [18, 19] that a diffusive behavior is only expected for low Q vectors, where the length scale is large compared to the jump size.

Figure 9 shows a slightly different dispersion constant C_{disp} for each system. This is due to the different Q space coverage of the systems and different averaging properties of the different pixel sizes and the crude approximation of an inversely proportional dispersion relation, which is purely empiric. However the stability

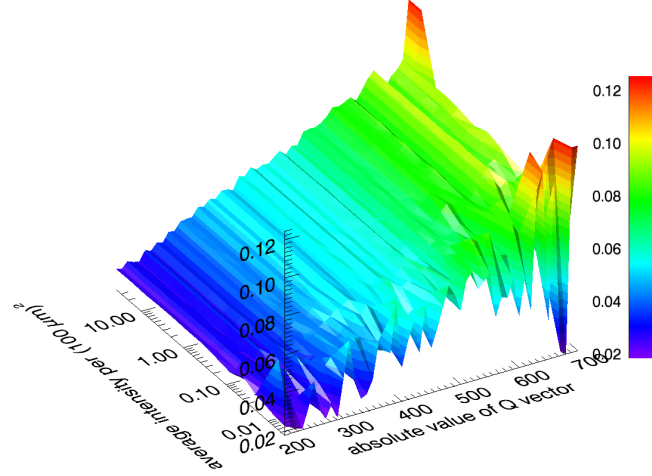


Figure 8: Inverse correlation time $\Gamma(Q)$ for the ideal $(100 \mu\text{m})^2$ detector and small ROIs as function of Q vector and intensity for photon statistics noise only. The results for the other detector systems look similar, but show larger variations.

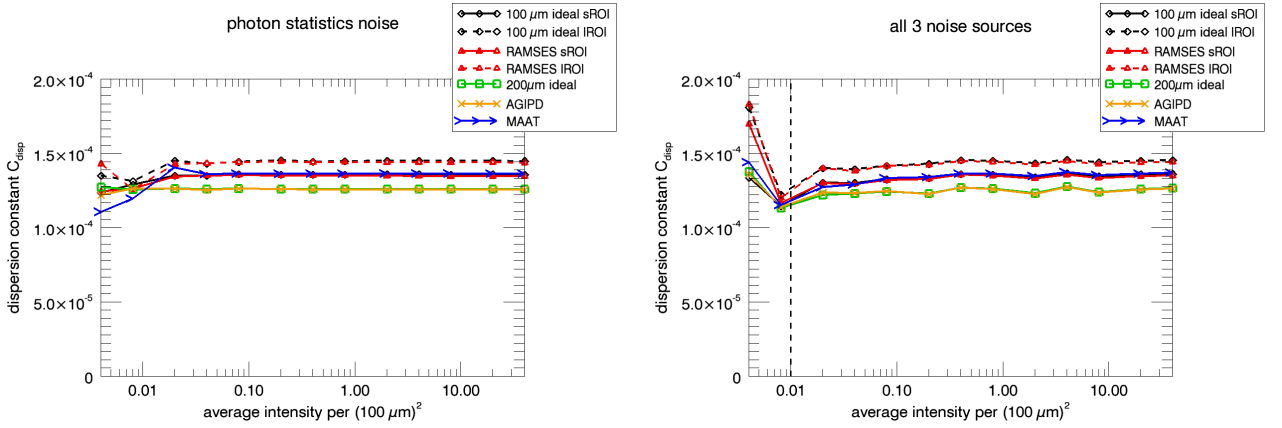


Figure 9: Dispersion constant C_{disp} for all detector systems as function of average intensity. The left image shows the results for photon statistics noise only, the right image shows the results including all mentioned noise contributions. The dashed vertical line indicates the average intensity of F_{noise} .

of the results as function of intensity show that this is merely a systematic error, which is identical for all systems of the same type, so it will not influence possible conclusions.

When evaluating the influence of the average intensity in Figure 9 one notices instabilities for the results at average intensities $\lesssim 0.01$. At these intensities no proper g_2 function could be built (shown in Figures 4 and 5). The extracted dispersion constant C_{disp} was observed to be more sensitive to these variations than the contrast. A reason for this might be the additional data evaluation step necessary to extract C_{disp} .

When evaluating the influence of the added incoherent noise by comparing the left to the right image in Figure 9 at average intensities $\gtrsim 0.02$, one notices very little effect. The reason of this is that the correlation time is independent of the contrast, as long as the contrast is high enough to reliably determine the correlation time.

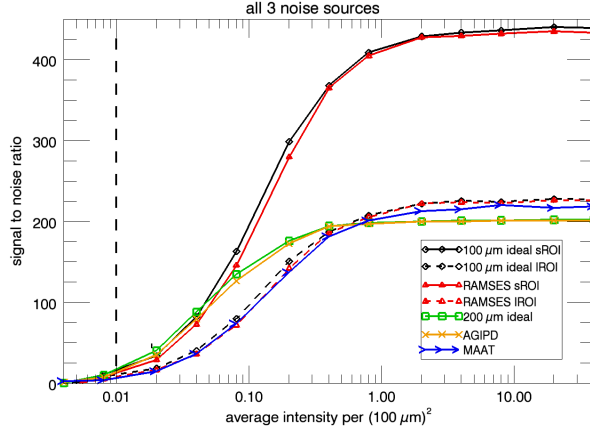


Figure 10: Signal to noise ratio for all detector systems as function of average intensity including all mentioned noise contributions. The shown curves have been determined for a Q value of 500, other Q values produce similar results. The dashed vertical line indicates the average intensity of F_{noise} .

5. Signal to noise ratio

The signal to noise ratio is commonly used as a figure of merit for XPCS experiments. Adapted to the situation of this study the analytic expression for the SNR, derived from the mean value of the g_2 function and its error ($err(g_2)$)¹⁰ is:

$$SNR(\langle I \rangle) = \frac{g_2 - 1}{err(g_2)} \propto \langle I_p \rangle C(\langle I \rangle) \sqrt{N} \quad (11)$$

with $\langle I_p \rangle$ being the average intensity in a pixel area, $C(\langle I \rangle)$ the optical contrast at this intensity and N the number of detector pixels.

Figure 10 shows the signal to noise ratio determined by dividing the first value ($k\Delta t = 1$) of the g_2 function minus 1 by its error determined from the variance of all g_2 functions at this lag time in the same Q space bin. This is the definition of the signal to noise ratio in the limit of small lag times as indicated in Equation 11. Figure 10 shows the signal to noise ratio at a fixed Q value of 500 (indicated by the dotted line in Figure 3). Evaluation of the signal to noise ratio at different Q values showed identical results.

The main features of Figure 10 are the increase with intensity for low intensities and the saturation of the SNR for high intensities. The saturation value is reached around average intensities of 1 photon per $(100 \mu\text{m})^2$. Additionally Figure 10 shows multiple separate sets of lines, one set for $(100 \mu\text{m})^2$ with small ROI, one set for large ROI and one set for $(200 \mu\text{m})^2$ systems. For low intensities the signal to noise ratio of the $(200 \mu\text{m})^2$ systems is approximately equal to the SNR of $(100 \mu\text{m})^2$ systems with small ROI and approximately twice the SNR of the $(100 \mu\text{m})^2$ systems with large ROI. Towards saturation all $(100 \mu\text{m})^2$ systems show larger SNRs than the $(200 \mu\text{m})^2$ systems, although only a little for large ROI and MAAT. The ratio of the SNR between large and small ROIs corresponds the square root of the ratio of the number of pixels. Ideal systems produce an SNR which is a little higher than that of the real systems due to their perfect quantum efficiency.

Equation 11 was derived under the assumption of low count rates and small contrast in the limit of small lag times ([7, 8] and references therein). A more elaborate derivation, also for large lag times, can be found in [17]. According to Equation 11 the SNR increases with intensity until the assumptions for its derivation are no longer valid.

¹⁰The error of the mean \bar{X} using N_s samples of a statistical population X is usually defined as $err(\bar{X}) = \sqrt{var_s(X)/N_s}$, where $var_s(X) = \frac{1}{N_s-1} \sum_i (X_i - \bar{X})^2$ is the variance of the N_s samples of X .

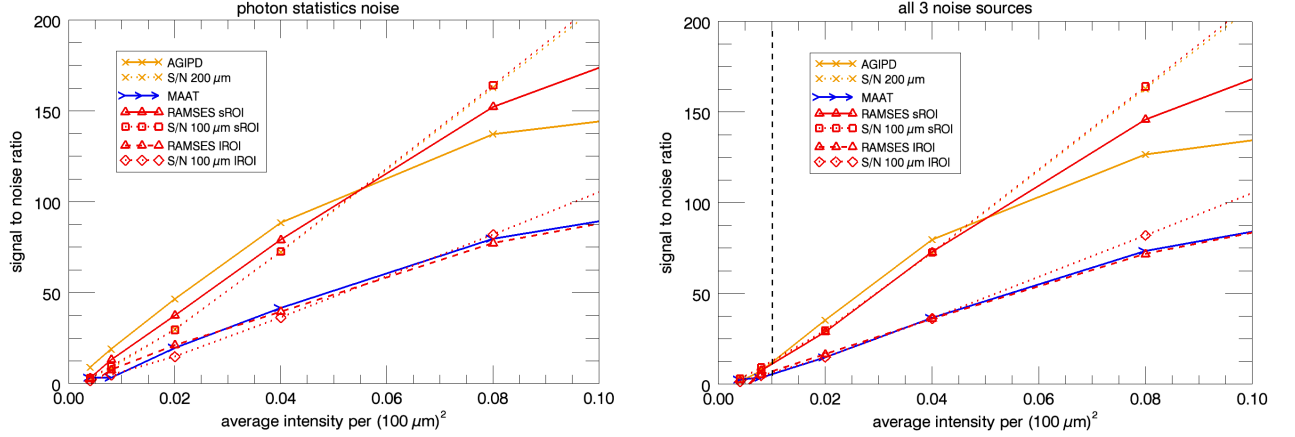


Figure 11: Signal to noise ratio for selected detector systems in the low intensity regime. The left image shows the results for photon statistics noise only, the right image shows the results including all mentioned noise contributions. The dashed vertical line indicates the average intensity of F_{noise} .

Using Equation 11 to compare the SNRs of two systems with linear pixel sizes P_1 and P_2 yields:

$$\frac{SNR_1(<I>)}{SNR_2(<I>)} = \frac{<I_1> C_1(<I>)}{<I_2> C_2(<I>)} \sqrt{\frac{N_1}{N_2}} \quad (12)$$

Assuming that the intensity in the pixel is proportional to its area and the intensity dependent terms of the contrast cancel, one can rewrite Equation 12 using Equation 10 as:

$$\frac{SNR_1}{SNR_2} = \frac{P_1^2 S^2 + P_2^2}{P_2^2 S^2 + P_1^2} \sqrt{\frac{N_1}{N_2}} \quad (13)$$

Equation 13 yields values from $\sqrt{N_1/N_2}$ for $P_1, P_2 \gg S$ to $(P_1/P_2)^2 \sqrt{N_1/N_2}$ for $P_1, P_2 \ll S$. For the systems investigated here Equation 13 yields the results observed for low intensities, namely

$SNR_{100\mu m, sROI}/SNR_{200\mu m} \approx 1.0$, $SNR_{100\mu m, lROI}/SNR_{200\mu m} \approx 0.5$ and

$SNR_{100\mu m, sROI}/SNR_{100\mu m, lROI} \approx 2.0$

Figure 11 shows the results for selected detector systems in the low intensity regime compared to the results from Equation 11. It can be seen that Equation 11 is a well suited approximation of the SNR at low intensities. Furthermore it can be seen, that for intensities below approximately 0.05 photons per $(100 \mu m)^2$ the signal to noise ratio of the AGIPD is larger than estimated from Equation 11.

6. Relative error E of the dispersion constant C_{disp}

The focus here is on a slightly different aspect of the error determination in XPCS experiments. As the main physical quantity of interest are the time constants connected with the dynamics the relative error in the time constants given by the ratio $E = \sqrt{var(C_{disp})}/C_{disp}$ was investigated. This quantity was derived by fitting the g_2 functions with the exponential correlation functions (Eq. 9). Thus E represents a different figure of merit than calculated by Equation 11. While for the SNR higher values indicate better quality, lower values of E indicate better values.

Both images of Figure 12 show a similar behavior in dropping from very large values at low intensities to a saturation value at high intensities. As already observed for the correlation time, the errors are very large for intensities $\lesssim 0.01$, indicating problems with the proper determination of the resulting quantities.

Comparing the left to the right image reveals the influence of the additional noise. While the data without additional noise is still usable at very low intensities the error increases significantly when the average intensity of the signal becomes comparable to the average noise intensity.

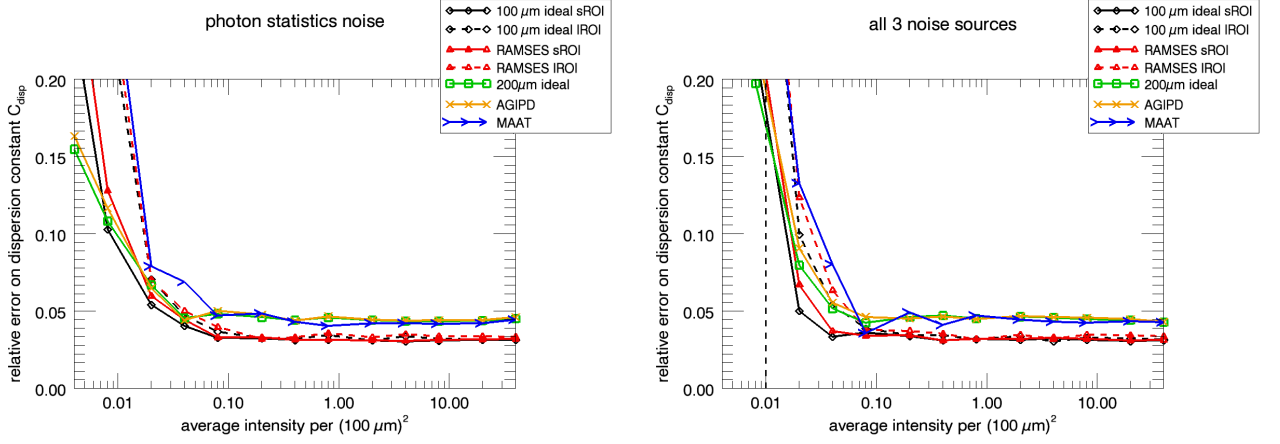


Figure 12: Relative error E of the dispersion constant C_{disp} for all detector systems as function of average intensity. The left image shows the results for photon statistics noise only, the right image shows the results including all mentioned noise contributions. The dashed vertical line indicates the average intensity of F_{noise} .

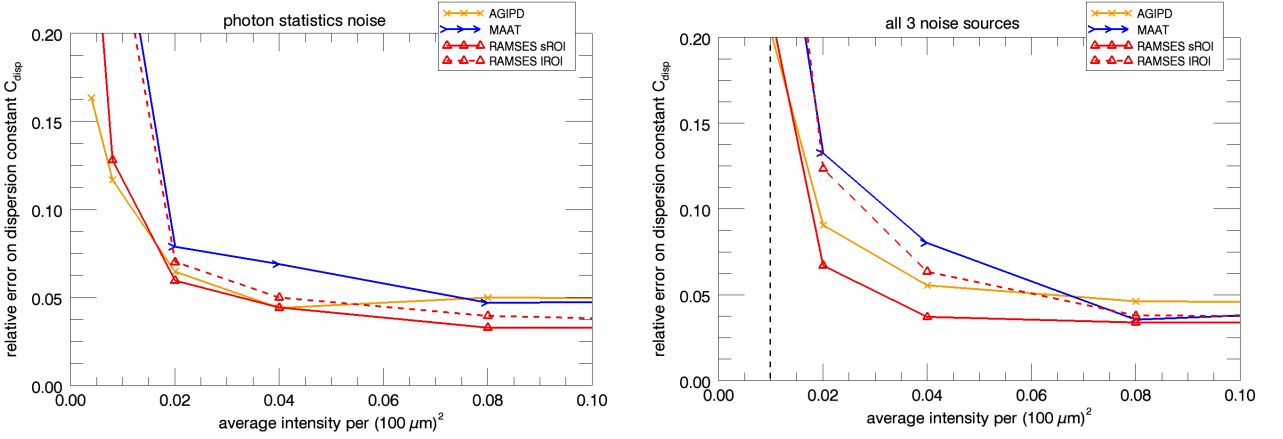


Figure 13: Relative error E of the dispersion constant C_{disp} for selected detector systems in the low intensity regime. The left image shows the results for photon statistics noise only, the right image shows the results including all mentioned noise contributions. The dashed vertical line indicates the average intensity of F_{noise} .

For average intensities above approximately 0.1 the results are independent of the noise. From this point on the systematic errors due to the artifacts in the g_2 functions caused by the limited number of frames dominate the results.

The saturation values are qualitatively different from the saturation values of the signal to noise ratio. The relative error saturates at lower intensities than the signal to noise ratio and to qualitatively different values, which result from the different numbers of pixels for the different detector systems, but do not show a \sqrt{N} behavior. The evaluated data is restricted to the Q range of 310 - 520 (shown in Figure 3), so the results were biased in favor of the $(100 \mu\text{m})^2$ detector systems, as more pixels were used for the evaluation than for the $(200 \mu\text{m})^2$ detectors.

Figure 13 shows the same data as Figure 12, but for low intensities on a linear scale.

For $F_{noise} = 0$ and low intensities the relative error E of all systems determined from the simulations is roughly equal.

When additional noise is present, the relative error E determined for RAMSES shows a \sqrt{N} dependence comparing large and small ROIs for $\langle I \rangle \leq 0.02$, which is not observed without noise. At higher

intensities this dependence vanishes as saturation sets in.

It is observed that for $\langle I \rangle \lesssim 0.05$ the relative error E of AGIPD is lower than the relative error determined for RAMSES and large regions of interest independently of the noise. It should be noted that the higher signal to noise ratio of AGIPD does not translate directly to a lower relative error.

7. Summary and discussion

A simulation tool using the detector simulation program HORUS was set up in order to simulate XPCS experiments. The numeric simulations took the whole chain, from a simple real space system and diffraction image generation via the detector response to the data evaluation, into account. It was shown that the simulated diffraction patterns show the counting statistics of fully coherent speckle patterns and have a well defined speckle size.

As method for data evaluation the well known intensity autocorrelation function was used and the most relevant parameters were extracted by a simple exponential fit to the g_2 function. The simulations were performed for a set of different detector systems assuming different noise sources.

Aperturing $(200 \mu\text{m})^2$ pixels to an effective size of $(100 \mu\text{m})^2$ increased the optical contrast. Although the signal to noise ratio was found to be similar to a natural $(100 \mu\text{m})^2$ system with the same number of pixels, the relative error was found to be worse than that of a detector system with natural $(100 \mu\text{m})^2$ pixels. Although, given enough intensity, the apertured system was not worse in terms of the relative error than a natural $(200 \mu\text{m})^2$ pixel system.

A decrease of optical contrast was observed for the non ideal systems and attributed to charge sharing effects.

The simulated intensity fluctuations had a very small effect on the data evaluation, which proved the robustness of the intensity autocorrelation technique and its applicability for experiments at free electron laser sources.

At larger intensities the simulation results for the signal to noise ratio and relative error saturated, in contrast to the expectations from analytic calculations.

In the intensity interval $\langle I \rangle / I_{\text{noise}} \lesssim 5$, the relative error was less and the SNR was larger when comparing $(200 \mu\text{m})^2$ pixel systems to $(100 \mu\text{m})^2$ pixel systems.

In this intensity region aperturing decreased the data quality, which has been shown by analytical calculations [20] using the signal to noise ratio.

The amount of simulated data (5 pulse trains) was limiting the precision of the results at the lowest intensities. Additional constraints were imposed by the limited number of acquired frames per pulse train. The systematic influences of this proved to be a restricting factor.

In the simulations the sample dynamics were completely independent of the illumination process. In experiments some of the incoming photons will always be absorbed by the sample and its suspending medium, giving rise to a temperature increase and possible changes in the sample. These effects were completely neglected in the simulations presented here, but might ultimately be the dominating effect for experiments at the European XFEL.

Furthermore in experimental situations many more complications may occur, e.g. partial coherence and anisotropic speckle sizes, which have been neglected here. The impact of those effects is beyond the scope of this study, but might influence the results for experiments at the European XFEL.

8. Conclusions

For low intensities the intuitive conclusion that aperturing is not beneficial as data is 'thrown away' was proven to be correct. For higher intensities aperturing was found to be beneficial, as charge sharing effects were excluded by it.

The error in the relevant determined physical parameters was shown to deviate in behavior from the signal to noise ratio.

Both signal to noise ratio and relative error saturated, but at different intensities.

Ultimately the use of simple fit functions and an insufficient number of frames limits the precision of this study.

At very low intensities AGIPD had a lower relative error and a higher signal to noise ratio than a system with the same number of pixels of $(100\text{ }\mu\text{m})^2$ size.

9. Acknowledgments

The authors would like to thank the European XFEL for funding of the development of AGIPD, as well as Anders Madsen from the European XFEL and Fabian Westermeier from the XPCS group at DESY for helping the corresponding author understand the XPCS technique. The simulations presented in this study use programming code that is based in parts on the HORUS program developed by Guillaume Potdevin [14], now at TU Munich.

References

- [1] M. Altarelli et al., European X-ray Free Electron Laser. Technical Design Report, ISBN 978-3-935702-17-1 (2006).
- [2] B. Henrich et. al., The adaptive gain integrating pixel detector AGIPD a detector for the European XFEL, Nucl. Instr. and Meth. A, DOI: 10.1016/j.nima.2010.06.107.
- [3] X. Shi et. al., Challenges in chip design for the AGIPD detector, Nucl. Instr. and Meth. A 624(2) 2010 387-391, DOI: 10.1016/j.nima.2010.05.038.
- [4] G. Potdevin et. al., Performance simulation of a detector for 4th generation photon sources: The AGIPD, Nucl. Instr. and Meth. A 607(1) 2009 51-54, DOI: 10.1016/j.nima.2009.03.121.
- [5] G. Grubel, F. Zontone, Correlation spectroscopy with coherent X-rays, J. Alloys and Compounds, DOI: 10.1016/S0925-8388(03)00555-3.
- [6] C. Gutt et. al., Measuring temporal speckle correlations at ultrafast x-ray sources, Optics Express 17(1) 2009 55-61.
- [7] E. Jakemen, in *Photon Correlation and Light Beating Spectroscopy*, Ch. 4, p. 75-150, H. Z. Cummins & E.R. Pike (Eds.), (Plenum, 1973).
- [8] P. Falus, L. B. Lurio, S. G. J. Mochrie, Optimizing the signal-to-noise ratio for X-ray photon correlation spectroscopy, J. Syn. Rad. 13(3) 2006 253-259, DOI:10.1107/S0909049506006789.
- [9] K. Hansen, M. Randall, S. Schleitner, C. Gutt, System-level simulation of a X-ray imager with nonlinear gain and per-pixel digitizer: XPCS case study, Nucl. Instr. and Meth. A 613(2) 2010 323-333, DOI: 10.1016/j.nima.2009.11.056.
- [10] G. Grübel, A. Madsen, and A. Robert in *Soft-Matter Characterization*, Ch. 18, p. 953-995, R. Borsali & R. Pecora (Eds.), (Springer, 2008).
- [11] R. F. Fowler, J. V. Ashby, C. Greenough, Computational modelling of semiconducting X-ray detectors, Nucl. Instr. and Meth. A 477(1-3) 2002 226-231, DOI: 10.1016/S0168-9002(01)01878-2.
- [12] Y. Chushkin, C. Caronna, A. Madsen, X-ray photon correlation spectroscopy of molecular dynamics using an event correlation scheme. Unpublished (2011).
- [13] J. Becker, E. Fretwurst, R. Klanner, Measurements of charge carrier mobilities and drift velocity saturation in bulk silicon of <111> and <100> crystal orientation at high electric fields, Solid-State Electronics, 56(1) 2011 104-110, DOI: 10.1016/j.sse.2010.10.009.
- [14] G. Potdevin, U. Trunk, H. Graafsma, HORUS, an HPAD X-ray detector simulation program, J. Inst. 4 2009 P09010, DOI: 10.1088/1748-0221/4/09/P09010.
- [15] J. Becker, D. Eckstein, R. Klanner, G. Steinbruck, Impact of plasma effects on the performance of silicon sensors at an X-ray FEL, Nucl. Instr. and Meth. A 615(2) 2010 230-236, DOI: 10.1016/j.nima.2010.01.082.
- [16] J. Becker, Signal development in silicon sensors used for radiation detection, PhD thesis, Hamburg University, July 2010, DESY-THESIS-2010-033.
- [17] K. Schatzel, Noise on Photon correlation data: I. Autocorrelation functions, Quantum Opt. 2 (1990) 287-305.
- [18] L. N. Gergidis, D. N. Theodorou and H. Jobic, Dynamics of n-Butane-Methane Mixtures in Silicalite, Using Quasielastic Neutron Scattering and Molecular Dynamics Simulations, J. Phys. Chem. B 104(23) 2000, 5541-5552, DOI: 10.1021/jp0000073.
- [19] C. T. Chudley and R. J. Elliott, Neutron Scattering from a Liquid on a Jump Diffusion Model, Proc. Phys. Soc. 77(2) 1961 353-361, DOI: 10.1088/0370-1328/77/2/319.
- [20] G. Grubel et. al., Report of Working Group II on X-ray Photon Correlation Spectroscopy, 2010, available at http://www.xfel.eu/sites/site_xfel-gmbh/content/e63594/e63599/e81232/e64013/e92121/MID-XPCS_Report_230610_eng.pdf